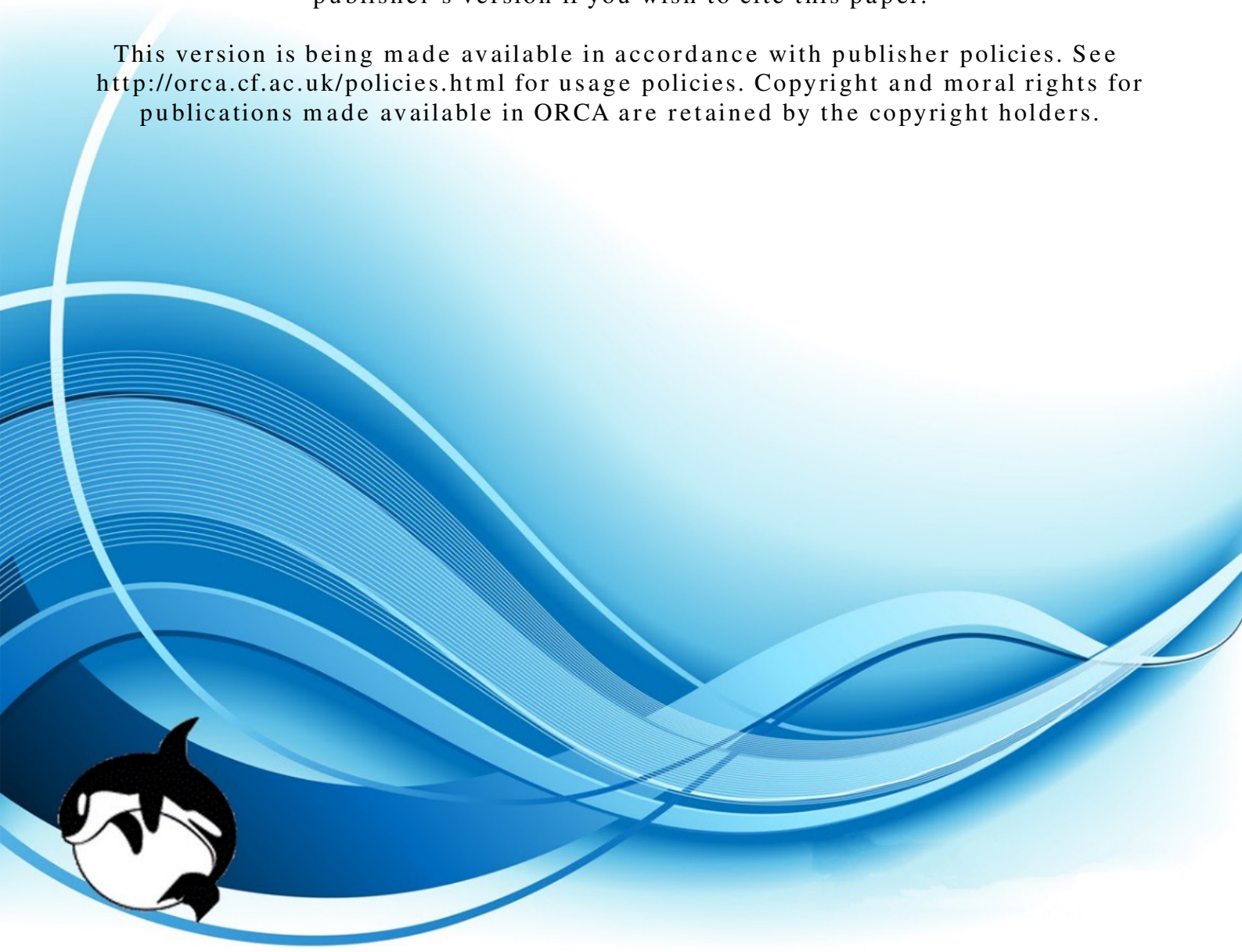

SPIRO: A Compliant Spiral Spring-Damper Joint Actuator with Energy-Based-Sliding-Mode Controller

Seyed Amir Tafrishi, *Member, IEEE,* Yasuhisa Hirata, *Member, IEEE,*

***Abstract*—Elasticity in actuators plays a crucial role in enabling flexible, efficient, and safe motion in robots. However, achieving such advanced capabilities also requires the development of sophisticated controllers. This paper introduces "SPIRO", a novel variable impedance actuator (patent-pending) capable of dynamically changing its stiffness and damping profiles to adapt to various tasks. We also propose a new energy-based-sliding-mode controller that facilitates robust stiffness and adaptive damping for intelligent actuator execution. Through experimental examples, we demonstrate how the compliance of the actuator can be adjusted based on the amount of disturbance energy, resulting in safer and more efficient motion. Moreover, the proposed mechanism, coupled with the designed controller, allows for a trade-off between accuracy and safety, enabling more dynamic link movements akin to human muscle. The unique capabilities of SPIRO make it promising for potential applications such as exoskeleton systems and human-robot interactions.**

***Index Terms*—Elastic joint, variable impedance actuator, spiral spring, nonlinear control**

I. Introduction

ACTUATORS are integral component of operating robots providing the necessary power and motion capabilities. However, conventional electric motors have limitations when it comes to tasks that require flexibility, energy efficiency, and safe interaction with the load side. For example, achieving optimal robot locomotion requires a delicate balance of stiffness and damping [1], [2]. This challenge becomes particularly significant when actuators need to directly interact with humans, such as in manipulators for active task support [3]–[5] or as assistive mechanisms in human locomotion [6]–[9]. This demand for a balance between safety and propulsion power/efficiency has led to the emergence of a new class of actuators known as variable impedance actuators (VIA).

VIAs are compliant mechanisms that utilize dedicated variable damping and stiffness to affect the transferred torque from the motor, with the sub-field of variable stiffness actuators (VSA) specifically focusing on real-time stiffness variation [10]. VIA offer various benefits for human-robot interaction applications [3], [11], as these compliant mechanisms can assist or interact with humans, eliminating the need for fixed conventional safeguards in classic human-robot interaction strategies. VIA with their existing spring profile or VSAs (sub-field mechanism) can conserve energy through compression of existing springs, enabling fast reactions for tasks such as throwing items by manipulators [12] or achieving efficient gait locomotion in legged robots [13].

VSA can conserve energy by utilizing spring deflection, and there are various strategies for integrating springs between the load and actuating motors [10]. Safety in this context involves redirecting/deflecting external forces that could be human-applied forces on the load side [3], [14], [15] or impacts from legged robot locomotion on the ground [1], [16]. However, spring compression can introduce challenges during the underdamped dynamics stage of the VSA mechanism, potentially causing instabilities [17]. Issues related to high velocities and stored energy have also been observed [18]. To address these challenges, recent studies have focused on developing control strategies for more efficient and safer VSAs. For example, Braun et al. proposed a new concept of positive-negative stiffness to suppress possible oscillations during underdamped motion [19]. In lower limb locomotion, spring-based compliant joints have been studied for stable trajectories and regenerative energy during motion [7]. However, some of these compensation strategies can over-complicate the issue and result in limited and bulky actuators that are challenging to implement in practice with to design more compact VSAs using vortex forms [20], [21].

Researchers have explored various approaches in the design of VIA to address limitations of VSA mechanisms [22]. For example, a piezoelectric friction damper integrated with a series elastic actuator [23] and multi-disc brake damping actuator [24] have been used as VSA. However, these mechanisms often require internal re-design of motor mechanics, which can be a practical drawback. Gunura et al. have developed a hot-melt adhesive with visco-elastic property as a powder brake to achieve variable damping [25]. Alternative attempts have been made to create variable impedance actuators using soft jamming brakes and artificial muscles to conserve elastic energy [26]. However, these joints are primarily designed as prismatic linear joint rather than revolute joint ones, which puts them at a disadvantage compared to conventional rotational joint actuators' broad practicality. Moreover, they often require a significant power source proportional to the load weight.

The presence of a spring component (stiffness) in a system can make it unstable, posing a classic problem in control theory [12], [21], [27]–[31]. Optimal controller methods have been applied to efficiently execute compliant actuators by releasing saved energy at the right time considering passivity [12], [27]. Robust sliding mode control, proposed by Wang [29], and methods combining energy-based approaches [12], [21], [28] have also been used for complex tasks under disturbance. Spyrakos et al. introduced the concept of passivity-preservation control (PPC) to address the challenge of variable impedance control due to induced energy-injecting elements in compliant systems [32]. While traditional passivity-based methods center around reducing the total system energy [32], [33], incorporating passivity with a controller that leverages an active damper profile has the potential to enhance convergence, making it more robust and dependable to incoming disturbance energy. Also, passive stiffness control relies on complex and bulky joint or end-effector structures, while active stiffness control demands torque sensing and intricate manipulation to achieve desired compliance, constraining their practicality and ease of implementation [34].

S. A. Tafrishi is with Engineering School, Cardiff University, Cardiff, UK (e-mail: Tafrishisa@cardiff.ac.uk).

Y. Hirata is with Department of Robotics, Tohoku University, Sendai, Japan (e-mail: hirata@srd.mech.tohoku.ac.jp).

This work was partially supported by Japan Science and Technology Agency (Moonshot R&D Program) under Grant JPMJMS2034.

Manuscript received April xx, 2023

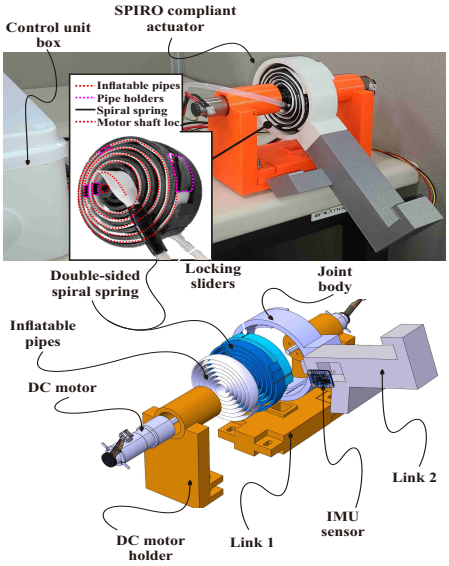

Fig. 1. SPIRO mechanism featuring a variable impedance actuator. The double-sided spiral spring is secured with sliding locks on both the joint body and the outer surface of the spiral spring (along the helical line).

In this work, we introduce "SPIRO," a compact compliant actuator capable of dynamically adjusting its impedance in response to external disturbances. We address limitations of prior variable stiffness actuators, which faced challenges like active stabilization issues and lacked easily designable damping profiles, especially for spiral spring models [3], [10], [14], [21]. The proposed mechanism achieves continuous stiffness modulation with precise control at the load-end due to dual-motor integration. It incorporates a novel variable damping element that operates efficiently without a need for large power sources [26]. This mechanism offers straightforward assembly, distinguishing it from earlier approaches [23], [24], and it does not rely on complex material compositions [25]. It also addresses hysteresis and the presence of a static friction band which was noted as drawback in friction dampers [22].

Moreover, previous studies overlooked the trade-off between safety and accuracy. This issue, for example, is a critical aspect of human muscle operation modes from a control perspective [35]. In that regard, muscles exhibit a dominant stiffness profile (resembling an under-damped system) for tasks requiring fast and responsive actions to achieve smooth and energy-efficient movements. However, for tasks demanding high accuracy and heightened safety measures (which may arise spontaneously), the damping profile becomes more persistent with a limited stiffness profile (resembling an over-damped system). To address this trade-off, we developed a new energy-based-sliding-mode controller that utilizes the adaptive impedance capabilities of the SPIRO mechanism to adjust its profile based on the situation and objective dynamically keeping the advantage of passivity.

The paper is organized as follows. First, we explain the mechanism of SPIRO with its model and its capabilities in Section II. In Section III, the problem statement of our control strategy is explained and a new energy-based sliding-mode controller considering a coupled robust stiffness and adaptive damping is proposed. Section IV demonstrate the experiment results and performance evaluation of a novel SPIRO mechanism with a designed new controller in point-to-point and trajectory tracking tasks. Finally, we conclude our findings in Section V.

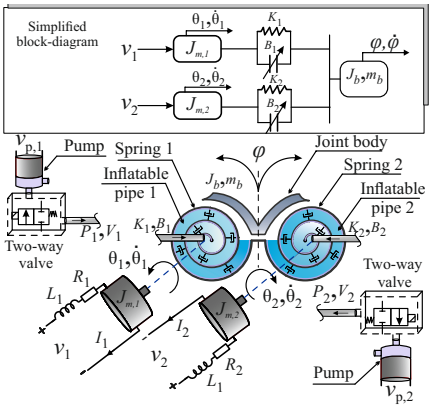

Fig. 2. Electrical and mechanical design of the SPIRO mechanism including the control unit box.

II. SPIRO Actuator Mechanism

In this section, we explain how the SPIRO mechanism is designed. Next, we describe the key features of this new variable impedance actuator.

A. Mechanism Design

The SPIRO mechanism, depicted in Fig. 1, introduces a novel variable impedance joint actuator. This mechanism comprises two main components: rigid double-sided spiral springs for variable stiffness, and soft inflatable pipes for variable damping. In Fig. 1, two DC Maxon motors (model: DCX22S GB KL 12V) equipped with absolute encoders (ENX16 EASY Absolute SSI) are directly connected to the double-sided spiral spring. Additionally, a current sensor (INA169) is incorporated for each DC motor. The double-sided spiral spring integrates two individual spiral springs, coupled at the outer end (Fig. 2). For this mechanism, a 3D-printed double-sided spiral spring, reinforced with nano-material within Poly Lactic Acid (PLA), imparts ample stiffness and facilitates force transmission between the load and motors. Each spring within the double-sided spiral configuration can be likened to a serial elastic actuator, offering the flexibility to adjust stiffness profiles at the load end (refer to Fig. 2). Furthermore, the spiral spring design allows for substitution with metal-based materials, enabling higher torque transfer capabilities. The stiffness constant of the spiral spring has been determined using [36]

$$K_c = \frac{\eta b_s d_t^3}{12 L_s}, \tag{1}$$

where η, b_s, d_t, L_s are Young's modulus, the width of spring, thickness and length of the spiral spring, respectively. Note that the values of the stiffness $K_c = 0.0958$ N/rad are validated with deflection and torque experiments.

The soft actuated element consists of inflatable pipes distributed along the helical lines of the spiral spring, as depicted in Fig. 1. These pipes are securely fixed at specific points (pipe holders) around the spiral spring lines to maintain their positions. Through a systematic inflation process, the pipes effectively dampen incoming forces between the joint body and motors, utilizing the interconnected spiral springs. In other words, the inflated pipes creates a direct force on helical lines of spiral spring with keeping high friction along the spiral distribution. For example, the pipes mostly constraining the inner helical line while keep the same force when is in tact with outer helical line (see Figs. 3-5). This damping mechanism plays a crucial role in achieving rapid stabilization, particularly

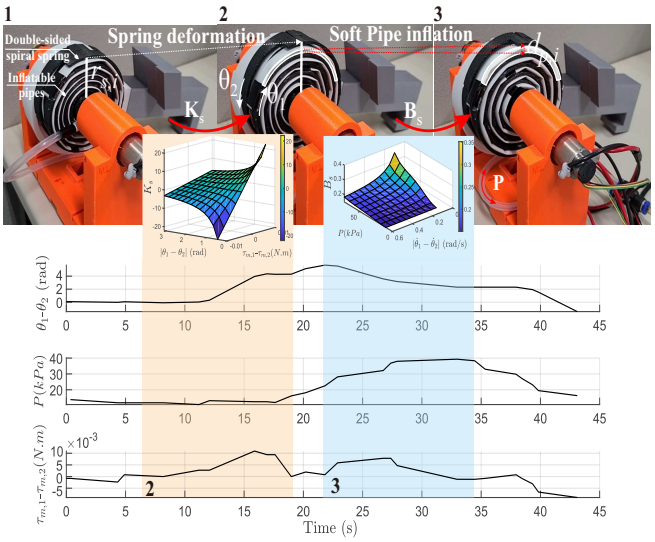

Fig. 3. Different functions by varying stiffness and damping profile of double-sided spiral spring. Plots illustrate the experiment shown in the video.

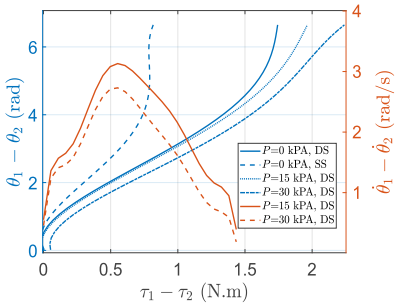

Fig. 4. The experimental identification of stiffness and damping profile of the SPIRO mechanism with using strain gauge sensor connected on the link.

in over-damped systems characterized by high stiffness profiles and substantial noise disturbances. In some sense, this can resemble the mechanical characteristics of human muscle operation. The mechanism can work either by changing the stiffness and damping independently or in a coupled state of stiffness and damping profiles similar to human muscle. Due to the simplicity of the primary mechanism, it can easily fit into conventional DC motors for applications in legged robots, exoskeleton systems or manipulators.

In this mechanism, DC motors with the angular orientation of $\mathbf{q}_m = [\theta_1, \theta_2]^T \in \mathbb{R}^2$ work in shifting the task of each side of a double-sided spiral spring as a power transmitter and impedance profile system or with a combination of all. Also, we have used an inertial measurement unit (IMU) with the Bno055 model to track link 2 accurately. From this sensor, we utilize both angular orientation and velocity $(\varphi, \dot{\varphi})$ (the main moving link). Fig. 2 illustrates the mechanical and electrical integration of the SIPRO mechanism. The spiral spring, as shown, is actuated by the rotation of two DC motors with PWM voltage inputs of $\mathbf{u}_m = [v_1,\ v_2]^T \in \mathbb{R}^2$. Also, the damping pipes are inflated by using 6 V 3 L/min miniature pump motors (voltage inputs of $\mathbf{u}_p = [v_{p,1}, v_{p,2}]^T$) with directly connected 6v two-way valves in the line of the fluid flow. The main reason for switching valves is to keep the pressure in the inflatable pipes as stable as possible. Because the aim is to have continuous control of the pressure of pipes to vary the damping effect with the volume change of soft pipes, we have created this fast switching valves and an exhaust valve. The exhaust valve is also used to limit the pressure while the fluid is pumped or empty a certain pressure level. It is important to note that these switches are miniature, and our SPIRO mechanism does not require any bulky compressor to keep the pressure stable and high in the inflatable pipes.

Next, it is important to explain the double-sided spiral spring's functions with attached damping pipes between the joint body and link 2 (shown in Fig. 1). By actuating electric motors, pump motors and valves in different ways, we have to change relative stiffness, damping and various capabilities, which is ruled by the following formulations

$$\begin{cases} \text{Joint rotation}: & \begin{cases} \dot{\varphi} \geq 0, & \left(\dot{\theta}_1(t) - \dot{\theta}_2(t)\right) \geq 0 \\ \dot{\varphi} < 0, & \left(\dot{\theta}_1(t) - \dot{\theta}_2(t)\right) < 0 \end{cases} \\ \text{Radius } r_s \text{ variation}: & \begin{cases} r_a \leq r_s(t), & (\theta_1(t) - \theta_2(t)) \geq 0 \\ r_a > r_s(t), & (\theta_1(t) - \theta_2(t)) < 0 \end{cases} \\ \text{Variable stiffness}: & \theta_1(t) \neq \theta_2(t), \quad K_s \approx 2K_c + \frac{\tau_{m,1} - \tau_{m,2}}{\theta_1 - \theta_2} \\ \text{Variable damping}: & \dot{\theta}_1(t) \neq \dot{\theta}_2(t), \ B_s \approx 2B_c + \frac{2A_p r_a P}{\dot{\theta}_1 - \dot{\theta}_2} d_p^{\frac{1}{2}} \end{cases} \quad (2)$$

where $\{K_c, B_c\}$ are the constant stiffness and damping values, P is the pressure in pipes, A_p area surface of the damping pipe, and r_a is the standard outer radius of the spiral spring. Please note that the following approximately illustrates the relevant stiffness and damping with primary analytical results. For instance, the outer radius of the spiral spring is considered as constant r_a value; however, radius r_a should be regarded as variable $r_s(t)$ if the current joint body does not exist (similarly shown in the video and Fig. 3). In the incoming section, we will obtain a more detailed formulation by considering all the contributing factors. To show the capability of the proposed SPIRO mechanism with the analytical formulation in (2), we present a simple test [1] as depicted in Fig. 3 where springs are in equilibrium without any external link connection. In the test, the mechanism is at rest with respect to electric motors and pumps, shown in case 1. In case 2, the angular orientation of motors happens in the opposite direction. This results in varying the stiffness and keeping the double-sided spiral spring in a new extended radius of r_s. The radius r_s can be arbitrarily changed and kept for the rest of the orientation while the new stiffness is achieved. Another ability is shown in case 3. The inflatable pipes are pumped with air until they get into satisfactory volume, which indicates relatively the amount of torque on the DC motors decreases (lesser current flow in motors). Thus, the deformed new spiral spring radius is kept in the same relative angular difference $(\theta_1 - \theta_2)$. Also, the extruded torque between two spiral springs that constructs the double-sided spiral spring $(\tau_{m,1} - \tau_{m,2})$ decreases the burden on the DC motor and changes the damping profile as another advantage. The overall behaviour of the developed SPIRO VIA mechanism is demonstrated with confirmed static experiments in Fig. 3.This validates the real-time adaptability of the SPIRO mechanism in modifying its stiffness and damping profiles. Also, the 3D plots depict the range of change in stiffness $K_s \in [-15, 15]$ N/rad and damping $B_s \in [0.1, 0.4]$ N·s/rad profile, including their constant values for currently designed spiral spring model with inflatable pipes. This range of variation in impedance profile illustrates the uniqueness of functional changes for designed SPIRO mechanism. Another

[1]The full demonstration is provided in the video.

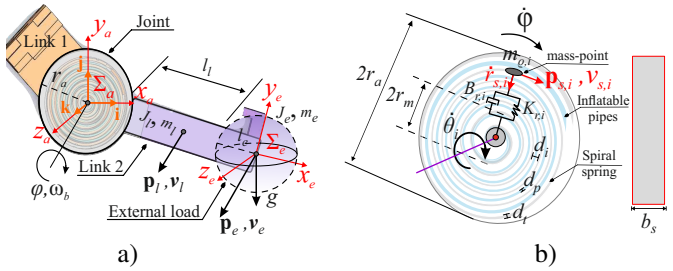

Fig. 5. a) The schematic of the SPIRO mechanism with connected links where Σ_e and Σ_a are the load and actuator (spiral spring centre) frames, b) Spring approximation model with mass-point particle $m_{\rho,i}$ motion with distance $r_{s,i}$ from the centre of frame Σ_a for estimating the damping coefficient. Also, damping inflatable pipes with diameter d_p have a radial distance from the spring by $d_i - d_p$ where d_i is two helical lines of spiral spring distance.

unique advantage of the mechanism is the ability to change the outer radius $r_s(t)$ (double-sided spiral spring resembles the wheel), which lets the SPIRO mechanism be both a joint actuator and a wheel-like actuator. The wheel actuator mode of the SPIRO and its transformation is a separate study (it is part of the patent-pending prototype), and we keep it for future studies for the sake of consistency in the current study.

Additionally, an identification test (Fig. 4) with an external link connected to a strain gauge sensor (KERN FH500) was conducted. Without pressure P in the inflatable damping pipes, the stiffness profile shifts completely when transitioning from a double-sided spring (DS) configuration to a single-sided (SS) one, where one spring is fixed and the other is rotated. This implies that we can determine a constant stiffness K_c for each spring (SS); however, the true stiffness K_s requires modification as presented in (2) when spring deflection shifts with motor control under different torques. Similarly, the activation of the damping pipe results in distinct profiles for the true damping B_s due to varying pressures. This means that the damping constant B_c contained within the spring will change relative to the pressure that inflatable pipes exert, as shown in (2). Additionally, the distance d_p between the damping pipes and spring helical lines is interpreted to accurately track the effect of damping on double-sided spring.

B. Dynamic Model of Actuator

At first, we find out the dynamics of the SPIRO mechanism with existing link connections as shown in Fig. 5. Let's assume the kinematics of the load on the end of the link Σ_e with respect to the actuator frame Σ_a is presented as Fig. 5. Then, we define the position of the joint system, including the i-th spiral spring, as follows:

$$\begin{aligned}
&\mathbf{p}_l = (r_a + \frac{l_l}{2})[\cos\varphi(t)\mathbf{i} + \sin\varphi(t)\mathbf{j}], \mathbf{p}_e = l[\cos\varphi(t)\mathbf{i} + \sin\varphi(t)\mathbf{j}],\\
&\mathbf{p}_{s,i} = r_{s,i}(t,\theta_i,\varphi)\big[\cos(\theta_i(t) - \varphi(t))\mathbf{i} + \sin(\theta_i(t) - \varphi(t))\mathbf{j}\big]
\end{aligned} \tag{3}$$

where $l = r_a + l_l + l_e$ is length from center of the joint till the external load and $r_{s,i}$ is changing radius of mass-point on the spiral spring. Then, by taking derivative of the Eq. (3), we obtain the kinematics as follows

$$\begin{aligned}
&\boldsymbol{v}_l = (r_a + \frac{l_l}{2})\dot{\varphi}\left[-\sin\varphi\mathbf{i} + \cos\varphi\mathbf{j}\right], \boldsymbol{v}_e = l\dot{\varphi}\left[-\sin\varphi\mathbf{i} + \cos\varphi\mathbf{j}\right],\\
&\boldsymbol{v}_{s,i} = \dot{r}_{s,i}(t,\theta_i,\varphi)\big[\cos(\theta_i - \varphi)\mathbf{i} + \sin(\theta_i - \varphi)\mathbf{j}\big]\\
&+ \Big(\dot{\theta}_i - \dot{\varphi}\Big)\Big[r_{s,i}(t,\theta_i,\varphi)\big[-\sin(\theta_i - \varphi)\mathbf{i} + \cos(\theta_i - \varphi)\mathbf{j}\big]\Big],\\
&\boldsymbol{\omega}_b = \dot{\varphi}\mathbf{k}, \;\; \boldsymbol{\omega}_{s,i} = (\dot{\theta}_i - \dot{\varphi})\mathbf{k}.
\end{aligned}$$

The link model is derived by using Lagrangian equations to include the load and connected joint models. Then, the kinetic energy for the rotating link T and rotating mass-point on spiral spring T_ϱ can be presented as follows

$$\begin{aligned}
&T = \frac{1}{2}\begin{bmatrix} \boldsymbol{v}_l^T \\ \boldsymbol{v}_e^T \end{bmatrix}\begin{bmatrix} m_l & 0 \\ 0 & m_e \end{bmatrix}\begin{bmatrix} \boldsymbol{v}_l \\ \boldsymbol{v}_e \end{bmatrix} + \frac{1}{2}\boldsymbol{\omega}_b^T\mathbf{J}_b\boldsymbol{\omega}_b + \frac{1}{2}\dot{\mathbf{q}}_m^T\mathbf{J}_m\dot{\mathbf{q}}_m,\\
&T_\varrho = \frac{1}{2}\begin{bmatrix} \boldsymbol{v}_{s,1}^T \\ \boldsymbol{v}_{s,2}^T \end{bmatrix}\begin{bmatrix} m_{\varrho,1} & 0 \\ 0 & m_{\varrho,2} \end{bmatrix}\begin{bmatrix} \boldsymbol{v}_{s,1} \\ \boldsymbol{v}_{s,2} \end{bmatrix},
\end{aligned}$$

where $\mathbf{J}_m = \mathbf{J}'_m + \mathbf{n}^2\mathbf{J}_g \in \mathbb{R}^{2\times2}$ that $\mathbf{J}'_m \in \mathbb{R}^{2\times2}$, $\mathbf{J}_g \in \mathbb{R}^{2\times2}$ and $\mathbf{n} = \text{diag}\{n_1, n_2\}$ are DC motor inertia, gear inertia and gear ratio. Next, the potential energy for the link U and mass-point on the spiral spring U_ϱ are

$$U = \frac{1}{2}\mathbf{q}_s^T\mathbf{K}_s\mathbf{q}_s + mg(1 - \cos\varphi),\; U_\varrho = \frac{1}{2}\mathbf{r}_s^T\mathbf{K}_r\mathbf{r}_s, \tag{4}$$

where $m = m_l(r_a + \frac{l_l}{2}) + m_e l$, and $\mathbf{K}_s = \text{diag}\{K_{s,1}, K_{s,2}\}$, $\mathbf{K}_r = \text{diag}\{K_{r,1}, K_{r,2}\}$, $\mathbf{q}_s = [(\theta_1 - \varphi),\;\; (\theta_2 - \varphi)]^T$, $\mathbf{q}_m = [\theta_1,\;\; \theta_2]^T$ are double-sided spiral spring stiffness on each side, the linear approximated stiffness of spring with mass-point model (shown in Fig. 5), relative orientations of spiral spring and electric motors orientation, respectively. Note that we have separated the energy of the mass-point system since this model will be used in the controller system design for indirect sensory information about spring deformation. Also, the energy model of the mass-point is very small that can be ignored for consideration as part of the total energy model of the system. The Lagrangian functions is found by $L = T - U$. Also, the viscous friction with a new definition of variable damping profiles for SPIRO mechanism P_s and mass-point P_ϱ are defined as

$$P_s = \frac{1}{2}\dot{\mathbf{q}}_m^T\mathbf{B}\dot{\mathbf{q}}_m + \frac{1}{2}\dot{\mathbf{q}}_s^T\mathbf{B}_d\dot{\mathbf{q}}_s,\; P_\varrho = \dot{\mathbf{r}}_s^T\mathbf{B}_r\dot{\mathbf{r}}_s, \tag{5}$$

while

$$\mathbf{B} = \mathbf{B}_m + \mathbf{n}^2\mathbf{B}_g \in \mathbb{R}^{2\times2},\; \mathbf{B}_d = \mathbf{B}_c + \mathbf{B}_p(t) \in \mathbb{R}^{2\times2}, \tag{6}$$

where $\mathbf{B}_m$, $\mathbf{B}_g$, $\mathbf{B}_c$ and $\mathbf{B}_p$ are constant motor and gear damping coefficients, and the constant damping coefficient in the spring-pipe model and our designed pipes variable damping value. Also, $\mathbf{B}_r$ will be an approximated linear spring-damping model with a mass-point end shown in Fig. 5 that solving the model will enable us to find the relative distance between the helical lines (d_i) in spiral spring in incoming sections. Then, the Lagrangian equations can be derived for the considered configuration of $\boldsymbol{x} = [\varphi,\; \mathbf{q}_m,\; \mathbf{r}_s]^T \in \mathbb{R}^5$ as follows

$$\frac{d}{dt}\left(\frac{\partial L}{\partial \dot{q}}\right) - \frac{\partial L}{\partial q} + \frac{\partial P}{\partial \dot{q}} = \tau, \tag{7}$$

where $[\mathbf{r}_s,\;\; \dot{\mathbf{r}}_s]$ are the displacement and velocity states for the mass-point m_{ϱ_i} on the spiral spring. By applying (7) to the derived Lagrangian functions $\{L,\; L_\varrho\}$ in L and viscous friction functions (5), we have following model

$$\mathbf{M}(\boldsymbol{x})\ddot{\boldsymbol{x}} + \mathbf{h}(\boldsymbol{x}, \dot{\boldsymbol{x}}) = \boldsymbol{\tau}, \tag{8}$$

where

$$\begin{aligned}
&\mathbf{M} = \begin{bmatrix} M_b & 0 & 0 \\ \mathbf{0} & \mathbf{J}_m & \mathbf{0} \\ \mathbf{0} & \mathbf{0} & \mathbf{m}_\varrho \end{bmatrix} \in \mathbb{R}^{5\times5},\; \mathbf{h} = [h_1, h_2, h_3, h_4, h_5]^T,\\
&\boldsymbol{\tau} = [\tau_{m,1} + \tau_{m,2},\; \tau_{m,1},\; \tau_{m,2},\; 0,\; 0]^T,
\end{aligned} \tag{9}$$

where $M_b = m_l(r_a + \frac{l_l}{2})^2 + m_e l_l^2 + J_l + J_e$ and also $\{m_l, J_l\}$ and $\{m_e, J_e\}$ consist of the mass and inertia of link and external object, respectively.

C. Electric Motor Model

The designed novel variable impedance actuator has two DC motors with gears ratios. We can show the motors electric model with the current states of $\mathbf{I}_m = [I_1,\ I_2]^T$ (as shown in Fig. 2) as follows

$$\dot{\mathbf{I}}_m = \mathbf{A}\boldsymbol{x}_m + \mathbf{B}\mathbf{u}_m, \tag{10}$$

where

$$\mathbf{A} = \begin{bmatrix} -\frac{R_1}{L_1} & 0 & -\frac{n_1\ K_{b,1}}{L_1} & 0 \\ 0 & -\frac{R_2}{L_2} & 0 & -\frac{n_2\ K_{b,2}}{L_2} \end{bmatrix},$$
$$\boldsymbol{x}_m = \begin{bmatrix} \mathbf{I}_m \\ \dot{\mathbf{q}}_m \end{bmatrix} \in \mathbb{R}^4, ; \mathbf{B} = \begin{bmatrix} \frac{1}{L_1} & 0 \\ 0 & \frac{1}{L_2} \end{bmatrix},\ \mathbf{u}_m = \begin{bmatrix} v_1 \\ v_2 \end{bmatrix},$$

where $\mathbf{u}_m$, L_i, R_i and $K_{b,i}$ are the i-th DC motor's voltage input, the armature inductance and the armature resistance and back emf constant, respectively.

D. The Spiral Spring Model

To accurately determine the damping effect of inflatable pipes in the design of our new mechanism, it is essential to determine the radial distance between the pipes and the deflecting spiral spring. The spring model plays a pivotal role in this process. To this end, we propose a solution that integrates spiral motion kinematics with inverse dynamics of rotating mass-point on spring to derive an indirect sensory input for calculating the distance between the helical lines of the deforming spiral spring. This approach facilitates effective estimation of the distance between the inflatable pipes and the spiral spring body.

At first, we use a discrete curve model of the spiral spring based on Fig. 5-b. The formulation is expressed by the Archimedean spiral model that the complete varying helical lines $\mathbf{p}_{a,i} \in \mathbb{R}^{2\times m}$ with a resolution of m are

$$\mathbf{p}_{a,i} = \mathbf{p}_0 + \boldsymbol{\Psi}\ (\bar{\mathbf{w}}\ \mathbf{r}_{s,i}), \tag{11}$$

where

$$\mathbf{p}_{a,i} = \begin{bmatrix} \mathbf{x}_{s,i} \\ \mathbf{y}_{s,i} \end{bmatrix},\ \mathbf{p}_0 = \begin{bmatrix} x_{0,i} \\ y_{0,i} \end{bmatrix}, \mathbf{r}_{s,i} = \frac{\boldsymbol{\Theta}}{2\pi n_{s,i}} r'_{s,i}(t),$$
$$\mathbf{w} = \begin{bmatrix} 1 \\ 1 \end{bmatrix},\ \boldsymbol{\Psi} = \begin{bmatrix} \cos(\boldsymbol{\Theta} + q_{s,i}) & \mathbf{0} \\ \mathbf{0} & \sin(\boldsymbol{\Theta} + q_{s,i}) \end{bmatrix}$$
$$\boldsymbol{\Theta} = [0, \cdots, \Theta_m]^T, \bar{\mathbf{w}} = [\ \mathbf{w}\ \ \cdots\ \ \mathbf{w}\ ]^T \in \mathbb{R}^{2m\times 1} \tag{12}$$

where $\Theta_m = 2\pi n_t$, $\boldsymbol{\Theta} \in \mathbb{R}^m$ and n_t are maximum angle of spiral, and angular steps vector and number of turns of spiral, and remaining variables in the model are determined by

$$n_{s,i}(r_{s,i}) = \frac{L_s}{\pi(r_{s,i}(t) - 2r_m)},\ r'_{s,i} = \frac{r_{s,i}(t)}{r_a}, q_{s,i} = \theta_i - \varphi. \tag{13}$$

It is important to note that we have considered a homogeneous distancing in (12); however, one can replace it with nonlinear forms to get more accurate results based on the material, tension and stiffness of spiral spring.

Next, to find changing value of $r_{s,i}(t)$ radius, we have to solve the differential equation for $(\dot{r}_{s,i}, r_{s,i})$ in (7) with the moving mass $(m_{\varrho,i})$ on spiral spring. By solving the following equation, we can have the axial motion toward the centre of the spiral spring, which gives the values for Eq. (13) parameters. Next, we should calculate the relative radial distance $\mathbf{d}_i$ between the inflated pipe and each of the spiral spring's helical gaps. This will determine the exerted force on the spiral spring when the damping pipes are inflated. This

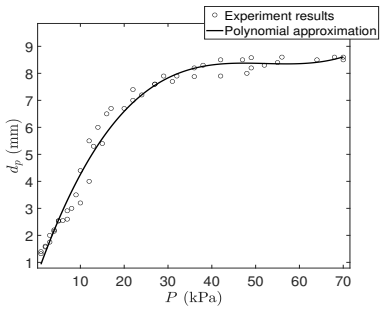

Fig. 6. The inflation distance vs the internal gauge pressure of inflatable damping pipes.

gap is important to know if the changing variable damping profile by the inflatable pipes is working simultaneously. The information of exerted forces will later be integrated into the variable damping coefficient $\mathbf{B}_p(t, \mathbf{d}_i)$. In this work, we assume the spring is deforming uniformly; hence, by taking two points on the spiral spring, we can determine the gap between arcs to know how much the inflatable pipes interact. For chosen arbitrary couple $(\Theta_1, r_{s,i}(\Theta_1))$ and $(\Theta_2, r_{s,i}(\Theta_2))$ of points on spring, we have

$$\mathbf{d}_d = \begin{bmatrix} d_{d,1} & 0 \\ 0 & d_{d,2} \end{bmatrix} + d_t\ \mathbf{I}_{2\times 2}, \tag{14}$$

where $d_{d,i} = \| \mathbf{p}_{a,i}(\Theta_1) - \mathbf{p}_{a,i}(\Theta_2) \|$ is Euclidean distance between two points $\{\Theta_1, \Theta_2\}$ in i-th spring, $\Theta_2 = 2k\pi + \Theta_1$ and d_t is the thickness of spiral spring's lines. As mentioned earlier, we made an approximation since there is non-linearity in spiral spring deformation (based on the chosen material). For instance, the parts near to centre will not have high flexibility for re-enforced PLA model of the SPIRO mechanism. Thus, we consider the maximum change in distance in our computation. One can obtain a more accurate model by including the rate of change for deformation to Eq. (12) or stiffness-dependent curvature parameters [37].

E. Fluid Actuated Variable Damper Model

In this study, the electric pump motors have a model with a constant fluid flow, while the pressure in pipes is measured from the pressure sensor. Then, we propose an approximated damping coefficient between the helical lines of the spiral spring and inflatable pipes of the SPIRO mechanism.

The damping coefficient $\mathbf{B}_p$ in (6) is defined for inflatable pipes (variable damper) with following

$$\mathbf{B}_p(\bar{\mathbf{P}}, \mathbf{d}_x, \dot{\bar{\mathbf{q}}}_s) = \begin{bmatrix} B_{p,1} & 0 \\ 0 & B_{p,2} \end{bmatrix} \triangleq \mathbf{r}_a \mathbf{F}_d \dot{\bar{\mathbf{q}}}_s^{-1} \mathbf{d}_x$$
$$= \begin{bmatrix} r_{a,1} & 0 \\ 0 & r_{a,2} \end{bmatrix} (\bar{\mathbf{P}}\mathbf{A}_p)\ \dot{\bar{\mathbf{q}}}_s^{-1} \mathbf{d}_x, \tag{15}$$

where $\mathbf{F}_d \in \mathbb{R}^{2\times 2}$, $\bar{\mathbf{P}} = \text{diag}\{P_1, P_2\}$, $\mathbf{A}_p = \text{diag}\{A_1, A_2\}$ are the force on spiral springs by pipe inflation, pressure in inflatable pipes and surface area on the pipe that touches the helical lines surface on spring, and also the true distance ratio is

$$\mathbf{d}_x = \left|\mathbf{I} - \mathbf{d}_r^{-1}\mathbf{d}_e\right|^{\frac{1}{2}} \tag{16}$$

while $\mathbf{d}_r$ and $\mathbf{d}_e$ are the standard radial gap distance between the two helical lines of spring and the true radial distance between the inflatable pipe and the helical line of spiral spring.

To determine the actual distance $\mathbf{d}_e$, we need to find the inflation distance of the pipes $\mathbf{d}_p$ first. To do this, we use a

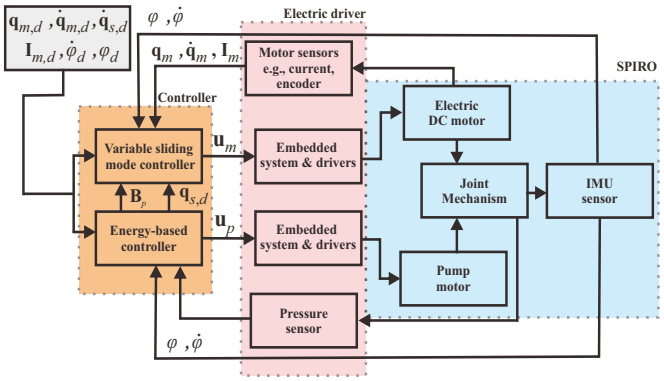

Fig. 7. Block diagram of the Energy-Based-Sliding-Mode Controller.

polynomial approximation model derived from experiments on a flattened pipe at normal atmospheric pressure of 101 kPa. Initially, we check the pressure in the internal gauge pressure, as shown in Fig. 6, for a constant length of pipe L_s. Next, the length of inflation $\mathbf{d}_p$ of the i-th inflatable pipe is defined by a third-order polynomial function approximation, which is expressed as:

$$d_{p,i} = c_1' P_i^3 + c_2' P_i^2 + + c_3' P_i + c_4', \tag{17}$$

where $[c_1',\ , c_2',\ c_3',\ c_4']$=$[5.68\times10^5,\ -0.0089,\ 0.461,\ 0.476]$. It is also clear from the figure that the pipe can extend maximum of 8.8 mm distance (semi-minor axis when deflated pipe is in ellipse form) pipe which is near to the circular diameter of the inflammable pipe.

Finally, based on the information, we can define the gap between inflatable pipe and the spiral spring line as follows:

$$\mathbf{d}_e = \mathbf{d}_p(\mathbf{P}) - \mathbf{d}(\mathbf{q}_s, \mathbf{r}_s), \tag{18}$$

where the distance between the inflatable pipes and deforming spiral spring lines $\mathbf{d}$ is defined as $\mathbf{d} = \mathbf{d}_d + \mathbf{d}_{safe}$ where $\mathbf{d}_d$ and $\mathbf{d}_{safe}$ are the actual distance of inflation pipe from (14) and constant of the safe distance of interaction.

III. The Controller

The proposed energy-based-sliding-mode controller is intended to control the variable impedance SPIRO actuator dynamically (refer to Fig. 7). The energy-based controller is designed to generate an adaptive damping profile on the actuator in response to different levels of disturbances/deviations, ensuring that the actuator remains stable and accurate at the desired configuration. The sliding mode controller, based on feedback from the energy-based controller, aims to converge the actuator to the desired states with adaptive stiffness, enabling the creation of safer, smoother, and energy-efficient motions for the links attached to the SPIRO actuator.

A. Problem Statement

Here, we explain our considered problem statement and how the controller is expected to work with the given desired configuration and disturbances.

This motion control problem aims to develop a strategy that mimics the mechanical behaviour of human muscles, using the variable impedance property to ensure the safe and accurate convergence of the SPIRO mechanism's actuation when faced with impulse disturbances or large push/pull. In this context, we define safety as a certain level of stiffness profile that provides the actuator with flexibility and softness during external disturbances caused by human/environmental interactions can be defined as passivity. Given the human-robot interaction component, this safety definition is particularly critical to the control strategy. Also, this approach leverages the physics of spring compression for efficiency, much like human muscles in cyclic motions such as running or moving. Accuracy, in turn, refers to point-to-point convergence (step references) with minimal fluctuation, which limits the stiffness profile by tuning the damping ratio, much like high-precision human muscle tasks. To address these requirements, we propose an energy-based-sliding-mode controller, as shown in Fig. 7, which enables interchangeably varying impedance through deviations from the desired configuration and energy of imposed disturbances.

The energy-based controller part is expected to minimize the incoming disturbances and increase the motion's accuracy by decreasing the spiral spring's effect during joint movement. The energy in the system is considered to be minimized in the spiral spring toward the desired values $\left(E_d,\ \dot{E}_d\right)$ by

$$E_d = \left[m_l(r_a + \frac{l_l}{2}) + m_e l\right] g(1 - \cos\varphi_d(t)), \tag{19}$$

where system total energy $E(t)$ is the potential energy of the double-sided spiral spring besides the energy due to the inertia and inductance of the motor $\{\mathbf{K}_s, \mathbf{J}_m, \mathbf{L}_m\}$. Also, we expect the spiral spring deflection in each motor will reach to desired angular deflection and velocity values $\left(\mathbf{q}_{s,d},\ \dot{\mathbf{q}}_{s,d}\right)$.

Next, the sliding-mode controller is expected to converge the desired states $(\varphi_d, \dot{\varphi}_d)$ of the link 2 , DC motors current $\mathbf{I}_{m,d}$, and spring deflection states $\left(\mathbf{q}_{s,d}, \dot{\mathbf{q}}_{s,d}\right)$ with changing the bounded voltage input in the DC motors $\mathbf{u}_m \in [-\mathbf{u}_{m,min},\ \mathbf{u}_{m,max}]$. The spring deflection states $(\mathbf{q}_s,\ \dot{\mathbf{q}}_s)$ are important since the sliding-mode controller aims to vary the spring deformation based on the current state of the SPIRO mechanism $\forall\{\boldsymbol{x}, \boldsymbol{x}_m\} \in \mathbb{R}^9$ to achieve variable stiffness. This problem requires the energy-based controller to adapt to the real-time variations of the spring deflection by changing the pressure input $\mathbf{u}_p \in [0,\ u_{p,max}]$ in damping pipes.

B. Energy-Based Controller for Adaptive Damping

The primary role of the energy-based controller is to adjust the damping of the SPIRO actuator in real-time as the connected link moves towards the desired configuration. The level of fluctuation in the convergence and the energy of external disturbances are used to generate a variable damping profile that gives a safe and robust convergence under disturbance considering passivity.

To derive the controller, we define the total energy of the system, including the kinetic and potential energies of the DC motor and the elastic joint connection as follows

$$E = \frac{1}{2}[\mathbf{q}_s\ \dot{\mathbf{q}}_m\ \mathbf{I}_m]^T \begin{bmatrix} \mathbf{K}_s & \mathbf{0} & \mathbf{0} \\ \mathbf{0} & \mathbf{J}_m & \mathbf{0} \\ \mathbf{0} & \mathbf{0} & \mathbf{L}_m \end{bmatrix} \begin{bmatrix} \mathbf{q}_s \\ \dot{\mathbf{q}}_m \\ \mathbf{I}_m \end{bmatrix}, \tag{20}$$

where $\mathbf{L}_m$= diag$\{L_1, L_2\}$. And, one will have the derivative of the energy function as

$$\dot{E} = [\mathbf{q}_s\ \dot{\mathbf{q}}_m\ \mathbf{I}_m]^T \begin{bmatrix} \mathbf{K}_s & \mathbf{0} & \mathbf{0} \\ \mathbf{0} & \mathbf{J}_m & \mathbf{0} \\ \mathbf{0} & \mathbf{0} & \mathbf{L}_m \end{bmatrix} \begin{bmatrix} \dot{\mathbf{q}}_s \\ \ddot{\mathbf{q}}_m \\ \dot{\mathbf{I}}_m \end{bmatrix}. \tag{21}$$

Next, to stabilize the SPIRO actuator and utilize a passivity in system behaviour, we propose following Lyapunov function for each pump motor $\mathbf{V}_e \in \mathbb{R}^2$ as follows

$$\mathbf{V}_e = \frac{1}{2}\mathbf{k}_e\tilde{E}^2 + \frac{1}{2}\mathbf{k}_d\mathbf{B}_d(\dot{\bar{\mathbf{q}}}_s - \dot{\bar{\mathbf{q}}}_{s,d})^2 + \frac{1}{2}\mathbf{k}_p\mathbf{K}_d(\bar{\mathbf{q}}_s - \bar{\mathbf{q}}_{s,d})^2, \tag{22}$$

where $\tilde{E} = E - E_d$ and we have introduced a robust stiffness $\mathbf{K}_d$ and adaptive damping $\mathbf{B}_d$ that are designed with respect to the controlled pressure in pipes by

$$\mathbf{K}_d \approx \mathbf{K}_c + \bar{\mathbf{q}}_s^{-1}\mathbf{A}_p\bar{\mathbf{P}}, \quad \mathbf{B}_d \approx \mathbf{B}_c + \dot{\bar{\mathbf{q}}}_s^{-1}\mathbf{A}_p\bar{\mathbf{P}}. \tag{23}$$

Then, by differentiating the Lyapunov function (22), we have

$$\dot{\mathbf{V}}_e = \underbrace{\mathbf{k}_e\tilde{E}\dot{\tilde{E}}}_{\boldsymbol{\vartheta}_e} + \underbrace{\frac{1}{2}\mathbf{k}_d\dot{\mathbf{B}}_d(\dot{\bar{\mathbf{q}}}_s - \dot{\bar{\mathbf{q}}}_{s,d})^2}_{\boldsymbol{\vartheta}_{d,1}} + \underbrace{\mathbf{k}_d\mathbf{B}_d(\dot{\bar{\mathbf{q}}}_s - \dot{\bar{\mathbf{q}}}_{s,d})\ddot{\bar{\mathbf{q}}}_s}_{\boldsymbol{\vartheta}_{d,2}} + \underbrace{\mathbf{k}_p\mathbf{K}_d(\bar{\mathbf{q}}_s - \bar{\mathbf{q}}_{s,d})\dot{\bar{\mathbf{q}}}_s}_{\boldsymbol{\vartheta}_p}. \tag{24}$$

After including pressure equations through the variable damping to the Eq. (24) one has

$$\begin{aligned}\dot{\mathbf{V}}_e = {} & \mathbf{k}_e\tilde{E}\Big(\mathbf{q}_s^T\mathbf{K}_s\dot{\mathbf{q}}_s + \dot{\mathbf{q}}_m^T(\mathbf{K}_m\mathbf{I}_m - \mathbf{h}_m) + \mathbf{I}_m^T\mathbf{L}_m(\mathbf{A}\boldsymbol{x}_m + \mathbf{B}\mathbf{u}_m) \\ & - \dot{E}_d\Big) + \mathbf{k}_d\Big[(\mathbf{B}_c + \dot{\bar{\mathbf{q}}}_s^{-1}\mathbf{A}_p\bar{\mathbf{P}})(\dot{\bar{\mathbf{q}}}_s - \dot{\bar{\mathbf{q}}}_{s,d})\bar{\mathbf{q}}_{sx} \\ & + \frac{1}{2}\left(-\bar{\mathbf{q}}_{sx}\dot{\bar{\mathbf{q}}}_s^{-2}\mathbf{A}_p + \dot{\bar{\mathbf{q}}}_s^{-1}\dot{\mathbf{A}}_p + \frac{1}{T}\dot{\bar{\mathbf{q}}}_s^{-1}\mathbf{A}_p\right)\bar{\mathbf{P}}(\dot{\bar{\mathbf{q}}}_s - \dot{\bar{\mathbf{q}}}_{s,d})^2 \\ & - \frac{1}{2}\dot{\bar{\mathbf{q}}}_s^{-1}\mathbf{A}_p\bar{\mathbf{P}}_{k-1}(\dot{\bar{\mathbf{q}}}_s - \dot{\bar{\mathbf{q}}}_{s,d})^2\Big] + \mathbf{k}_p\left(\mathbf{K}_c + \bar{\mathbf{q}}_s^{-1}\mathbf{A}_p\bar{\mathbf{P}}\right)(\bar{\mathbf{q}}_s - \bar{\mathbf{q}}_{s,d})\dot{\bar{\mathbf{q}}}_s,\end{aligned}$$

where

$$\mathbf{K}_m = \begin{bmatrix} k_{m,1} & 0 \\ 0 & k_{m,2} \end{bmatrix}, \ \mathbf{q}_{sx} = \ddot{\bar{\mathbf{q}}}_s,$$
$$\ddot{\bar{\mathbf{q}}}_s = \mathbf{J}_m^{-1}(\mathbf{K}_m\mathbf{I}_m - \mathbf{h}_m) - \mathbf{w}\left(\mathbf{K}_m^T\mathbf{I}_m - h_1\right).$$

while $\bar{\mathbf{P}} = \bar{\mathbf{P}}_k$ and $\bar{\mathbf{P}}_{k-1}$ is the previous step's pressure in inflatable damping pipes and we assume the rate of change in pressure based on sampling frequency is lower, hence, one has $\dot{\bar{\mathbf{P}}} = \frac{1}{T}(\bar{\mathbf{P}}_k - \bar{\mathbf{P}}_{k-1})$. By finding the Lyapunov function as $\dot{\mathbf{V}}_e = \mathbf{0}$ for the pressure $\bar{\mathbf{P}}$, we have

$$\begin{aligned}\bar{\mathbf{P}} = {} & -\Big[\mathbf{k}_d\dot{\bar{\mathbf{q}}}_s^{-1}\mathbf{A}(\dot{\bar{\mathbf{q}}}_s - \dot{\bar{\mathbf{q}}}_{s,d})\bar{\mathbf{q}}_{sx} + \mathbf{k}_p\bar{\mathbf{q}}_s^{-1}\mathbf{A}(\bar{\mathbf{q}}_s - \bar{\mathbf{q}}_{s,d})\dot{\bar{\mathbf{q}}}_s \\ & + \frac{1}{2}\mathbf{k}_d\left(-\bar{\mathbf{q}}_{sx}\dot{\bar{\mathbf{q}}}_s^{-2}\mathbf{A} + \dot{\bar{\mathbf{q}}}_s^{-1}\dot{\mathbf{A}} + \frac{1}{T}\dot{\bar{\mathbf{q}}}_s^{-1}\mathbf{A}\right)(\dot{\bar{\mathbf{q}}}_s - \dot{\bar{\mathbf{q}}}_{s,d})^2\Big]^{-1} \\ & \cdot \Big[\mathbf{k}_e\tilde{E}\Big(\mathbf{q}_s^T\mathbf{K}_s\dot{\mathbf{q}}_s + \dot{\mathbf{q}}_m^T(\mathbf{K}_m\mathbf{I}_m - \mathbf{h}_m) \\ & + \mathbf{I}_m^T\mathbf{L}_m(\mathbf{A}\boldsymbol{x}_m + \mathbf{B}\mathbf{u}_m) - \dot{E}_d\Big) + \mathbf{k}_d\Big[\mathbf{B}_c(\dot{\bar{\mathbf{q}}}_s - \dot{\bar{\mathbf{q}}}_{s,d})\bar{\mathbf{q}}_{sx} \\ & - \frac{1}{2}\dot{\bar{\mathbf{q}}}_s^{-1}\mathbf{A}\bar{\mathbf{P}}_{k-1}(\dot{\bar{\mathbf{q}}}_s - \dot{\bar{\mathbf{q}}}_{s,d})^2\Big] + \mathbf{k}_p\mathbf{K}_c(\bar{\mathbf{q}}_s - \bar{\mathbf{q}}_{s,d})\dot{\bar{\mathbf{q}}}_s\Big].\end{aligned}$$

The variable damping with pressure control has singular points (resulting the control input $\bar{\mathbf{P}}$ to converge to zero even when $[\mathbf{q}_s, \dot{\mathbf{q}}_s] < \boldsymbol{\epsilon}$]) that requires to be eliminated during the execution; hence, we have come up with following conditional formulation of

$$\begin{aligned}\bar{\mathbf{P}} = {} & -\Big(\mathbf{k}_d\dot{\mathbf{Q}}_s + \mathbf{k}_p\mathbf{Q}_s\Big)^{-1}\Big[\mathbf{k}_e\tilde{E}\Big(\mathbf{q}_s^T\mathbf{K}_s\dot{\mathbf{q}}_s + \dot{\mathbf{q}}_m^T(\mathbf{K}_m\mathbf{I}_m - \mathbf{h}_m) \\ & + \mathbf{I}_m^T\mathbf{L}_m(\mathbf{A}\boldsymbol{x}_m + \mathbf{B}\mathbf{u}_m) - \dot{E}_d\Big) + \mathbf{k}_d\Big[\mathbf{B}_c(\dot{\bar{\mathbf{q}}}_s - \dot{\bar{\mathbf{q}}}_{s,d})\bar{\mathbf{q}}_{sx} \\ & - \frac{1}{2}\dot{\bar{\mathbf{q}}}_s^{-1}\mathbf{A}\bar{\mathbf{P}}_{k-1}(\dot{\bar{\mathbf{q}}}_s - \dot{\bar{\mathbf{q}}}_{s,d})^2\Big] + \mathbf{k}_p\mathbf{K}_c(\bar{\mathbf{q}}_s - \bar{\mathbf{q}}_{s,d})\dot{\bar{\mathbf{q}}}_s\Big].\end{aligned} \tag{25}$$

where

$$\mathbf{Q}_s \triangleq \begin{cases} \bar{\mathbf{q}}_s^{-1}\mathbf{A}(\bar{\mathbf{q}}_s - \bar{\mathbf{q}}_{s,d})\dot{\bar{\mathbf{q}}}_s, & |\mathbf{q}_s(t)| \le \mathbf{q}_{s,max} \\ \bar{\mathbf{q}}_{s,\max}^{-1}\mathbf{A}(\bar{\mathbf{q}}_s - \bar{\mathbf{q}}_{s,d})\dot{\bar{\mathbf{q}}}_s, & |\mathbf{q}_s(t)| > \mathbf{q}_{s,max} \end{cases}$$

$$\dot{\mathbf{Q}}_s \triangleq \begin{cases} \dot{\bar{\mathbf{q}}}_s^{-1}\big[\mathbf{A}(\dot{\bar{\mathbf{q}}}_s - \dot{\bar{\mathbf{q}}}_{s,d})\bar{\mathbf{q}}_{sx} + \frac{1}{2}\big(-\bar{\mathbf{q}}_{sx}\dot{\bar{\mathbf{q}}}_s^{-1}\mathbf{A} + \dot{\mathbf{A}} \\ \quad + \frac{1}{T}\mathbf{A}\big)(\dot{\bar{\mathbf{q}}}_s - \dot{\bar{\mathbf{q}}}_{s,d})^2\big], & |\dot{\mathbf{q}}_s(t)| \le \dot{\mathbf{q}}_{s,max} \\ \dot{\bar{\mathbf{q}}}_{s,max}^{-1}\big[\mathbf{A}(\dot{\bar{\mathbf{q}}}_{s,max} - \dot{\bar{\mathbf{q}}}_{s,d})\bar{\mathbf{q}}_{sx} + \frac{1}{2}\big(-\bar{\mathbf{q}}_{sx}\dot{\bar{\mathbf{q}}}_{s,max}^{-1}\mathbf{A} \\ \quad + \dot{\mathbf{A}} + \frac{1}{T}\mathbf{A}\big)(\dot{\bar{\mathbf{q}}}_{s,max} - \dot{\bar{\mathbf{q}}}_{s,d})^2\big], & |\dot{\mathbf{q}}_s(t)| > \dot{\mathbf{q}}_{s,max} \end{cases}$$

Eq. (25) can present the direct pressure control through the following $\mathbf{u}_p = R_s\,\bar{\mathbf{P}}\mathbf{w} \in \mathbb{R}^2$ where R_s is the softness ratio. The softness ratio R_s allows for different flexibility ranges for the SPIRO mechanism based on the task.

We now check the stability of the adaptive damper with the given energy-based controller in the proposed Lyapunov function (24). Let's assume the function's energy term is bounded (21) due to the maximum deflection angle $\mathbf{q}_s \in [-\mathbf{q}_{s,max}, \mathbf{q}_{s,max}]$ and velocity $\dot{\mathbf{q}}_s \in [-\dot{\mathbf{q}}_{s,max}, \dot{\mathbf{q}}_{s,max}]$ and similar properties on the motor states $\boldsymbol{x}_m \le \boldsymbol{x}_{max}$; then, the function candidate $\mathbf{V}_e$ should be stable around equilibrium $\{\mathbf{q}_{s,d}, \dot{\mathbf{q}}_{s,d}\}$ with satisfying LaSalle's theorem. It can be seen the function in Eq. (22) is positive definite; thus, we can have the following condition for stable convergence

$$\dot{\mathbf{V}}_e(\boldsymbol{x}, \boldsymbol{x}_m) \le \mathbf{0}, \quad \forall\{\boldsymbol{x}, \boldsymbol{x}_m\} \in \mathbb{R}^9. \tag{26}$$

Eq. (24) gives a better understanding of which terms are negative with considering the inequality (26). In (24), we have the energy term as $\boldsymbol{\vartheta}_e \in \mathbb{R}^2 < \mathbf{0}$ since the desired energy E_d will have certain positive value due to gravity on the link. Another term about the variable damping that is designed by $\mathbf{B}_d$ shows that $\boldsymbol{\vartheta}_{d,1} \in \mathbb{R}^2 < \mathbf{0}$ term is strictly negative because its sub-term is $\dot{\mathbf{B}}_d < \mathbf{0}$. The term $\boldsymbol{\vartheta}_p$ is a variable with the continuous sign change, which confirms a gain design inequality as $\mathbf{k}_p < \mathbf{k}_e + \mathbf{k}_d$. This gain condition will make the controller stays in a stable region while disturbance or deflection exists in the spiral spring.

C. Sliding Mode Controller for Adaptive Stiffness

The main link connected to the SPIRO mechanism is controlled using a new adaptive sliding mode controller that adjusts its internal variables. We employ this controller for the DC motors to ensure convergence of the link configuration $(\varphi, \dot{\varphi})$, motor states $(\mathbf{I}_m, \dot{\mathbf{q}}_m)$, and spring deflection $(\mathbf{q}_s, \dot{\mathbf{q}}_s)$ to desired states. Subsequently, we define our sliding surface as follows:

$$\begin{aligned}\mathbf{S} = \begin{bmatrix} s_1 \\ s_2 \end{bmatrix} = {} & \mathbf{C}_1\mathbf{w}(\varphi - \varphi_d) + \mathbf{C}_2\mathbf{w}(\dot{\varphi} - \dot{\varphi}_d) \\ & + \mathbf{C}_3(\mathbf{I}_m - \mathbf{I}_{m,d}) + \mathbf{C}_4(\mathbf{q}_s - \mathbf{q}_{s,d}) + \mathbf{C}_5(\dot{\mathbf{q}}_s - \dot{\mathbf{q}}_{s,d}),\end{aligned}$$

where the gain $\mathbf{C}_i$ for each term is presented as follows

$$\mathbf{C}_i = \begin{bmatrix} c_{i,1} & 0 \\ 0 & c_{i,2} \end{bmatrix} \in \mathbb{R}^{2\times 2}. \tag{27}$$

Note that we assume the motor final position is not important in this problem. Then, by taking the derivative we have

$$\dot{\mathbf{S}} = \mathbf{C}_1\mathbf{w}\left(\dot{\varphi}-\dot{\varphi}_d\right) + \mathbf{C}_2\mathbf{w}\ \ddot{\varphi} + \mathbf{C}_3\left(\dot{\mathbf{I}}_m - \dot{\mathbf{I}}_{m,d}\right) + \mathbf{C}_4\left(\dot{\mathbf{q}}_s - \dot{\mathbf{q}}_{s,d}\right) + \mathbf{C}_5\left(\ddot{\mathbf{q}}_s - \ddot{\mathbf{q}}_{s,d}\right). \tag{28}$$

Now, one can design the control input with the following definition of sliding surface

$$\dot{\mathbf{S}} = -\mathbf{K}\ \mathrm{sgn}(\mathbf{S}), \tag{29}$$

where $\mathbf{K} \in \mathbb{R}^{2\times 2}$ is the positive gain. Now, by equaling (28) and (29), one can find the controller for the motors

$$\mathbf{u}_m = -\mathbf{L}_m\mathbf{C}_3^{-1}\Big[\mathbf{K}\ \mathrm{sgn}(\mathbf{S}) + \mathbf{C}_1\mathbf{w}\left(\dot{\varphi}-\dot{\varphi}_d\right) + \mathbf{C}_2\mathbf{w}\left(\mathbf{w}^T\mathbf{K}_m\mathbf{I}_m - h_1\right) + \mathbf{C}_3\left(\mathbf{A}\mathbf{x}_m - \dot{\mathbf{I}}_{m,d}\right) + \mathbf{C}_4\left(\dot{\mathbf{q}}_s - \dot{\mathbf{q}}_{s,d}\right) + \mathbf{C}_5\Big(\mathbf{J}_m^{-1}\left(\mathbf{K}_m\mathbf{I}_m - \mathbf{h}_q\right) - \frac{1}{M_b}\mathbf{w}\left(\mathbf{w}^T\mathbf{K}_m\mathbf{I}_m - h_1\right) - \ddot{\mathbf{q}}_{s,d}\Big)\Big],$$

where $\mathbf{h}_q = [h_2,\ h_3]^T$.

The stability of the proposed control strategy can be considered first based on the singular point that we have, which is only on the motor inductance and electrical motor term that create a direct constraint on the value of $\mathbf{C}_3 \ll \mathbf{L}_m/\boldsymbol{\sigma}$ gain

$$\mathbf{L}_m\mathbf{C}_3^{-1} \ll \boldsymbol{\sigma}, \tag{30}$$

where $\boldsymbol{\sigma} \in \mathbb{R}^2$ is a small value. Then, supposing the boundedness of states, the stability of the controller with continuously changing values in the two variables of the desired angular deflection and adaptive damping $\left(\mathbf{q}_{s,d},\ \mathbf{B}_p\right)$ the chosen Lyapunov function can look at

$$\mathbf{V}_s = \frac{1}{2}\mathbf{S}^2(\mathbf{q}_{s,d}), \tag{31}$$

then, taking the derivative of the function results in following

$$\dot{\mathbf{V}}_s = \mathbf{S}(\mathbf{q}_{s,d})\dot{\mathbf{S}}(\mathbf{B}_p) = \mathbf{S}(\mathbf{q}_{s,d})\big[\mathbf{C}_1\mathbf{w}(\varphi-\varphi_d) + (\mathbf{C}_2-\mathbf{C}_5)\,\mathbf{w}\ddot{\varphi}(\mathbf{B}_p) + \mathbf{C}_3\dot{\mathbf{I}}_m + \mathbf{C}_4\dot{\mathbf{q}}_s + \mathbf{C}_5\ddot{\mathbf{q}}_m(\mathbf{B}_p)\big] \le -\mathbf{K}\ \mathrm{sgn}(\mathbf{S}).$$

It is straightforward to verify whether the changing desired deflection is bounded, as the springs have a maximum deflection of $\mathbf{q}_s < \mathbf{q}_{s,max}$. This implies that $\mathbf{S}(\mathbf{q}_{s,d}(t)) \le \mathbf{S}(q_{s,max})$. Consequently, $-\mathbf{K}\mathrm{sgn}(\mathbf{S})$ will always follow the same direction of convergence with $\mathbf{S}(\mathbf{q}_{s,d})$, but the gain $\mathbf{K}$ must satisfy the constraints of the remaining terms in $\dot{\mathbf{S}}(\mathbf{B}_p)$, which are limited by the maximum damping torque exerted on the joint, $\mathbf{B}_{p,max}$. Therefore, taking into account the bounded changes in terms resulting from the energy-based controller, we obtain the following inequality:

$$\mathbf{S}(\mathbf{q}_{s,d})\big[\mathbf{C}_1\mathbf{w}(\dot{\varphi}-\dot{\varphi}_d) + (\mathbf{C}_2-\mathbf{C}_5)\,\mathbf{w}\ddot{\varphi}(\mathbf{B}_p) + \mathbf{C}_3\dot{\mathbf{I}}_m + \mathbf{C}_4\dot{\mathbf{q}}_s + \mathbf{C}_5\ddot{\mathbf{q}}_m(\mathbf{B}_p)\big] \le \big|\mathbf{S}(\mathbf{q}_{d,max})\big|\ \big[\,(\mathbf{C}_1-\mathbf{C}_4)\,\mathbf{w}\dot{\varphi} - \mathbf{C}_1\mathbf{w}\dot{\varphi}_d + (\mathbf{C}_2-\mathbf{C}_5)\,\mathbf{w}\ddot{\varphi}(\mathbf{B}_{p,max}) + \mathbf{C}_3\dot{\mathbf{I}}_m + \mathbf{C}_4\dot{\mathbf{q}}_m + \mathbf{C}_5\ddot{\mathbf{q}}_m(\mathbf{B}_{p,max})\big] \le \mathbf{K}, \tag{32}$$

and, designing the gains as $\mathbf{C}_2 < \mathbf{C}_5$, $\mathbf{C}_4 < \mathbf{C}_1$ and $\mathbf{C}_3 < \boldsymbol{\sigma}$, we can the simplify inequality shown in (32) in a reduced form as follows

$$\big|\mathbf{S}(\mathbf{q}_{d,max})\big|\ \big[-|\mathbf{C}_1\mathbf{w}\dot{\varphi}_d + \mathbf{C}_4\dot{\mathbf{q}}_m + \mathbf{C}_5\ddot{\mathbf{q}}_m(\mathbf{B}_{p,max})|\ \big] < \big|\mathbf{S}(\mathbf{q}_{d,max})\big|\ \big[-\mathbf{C}_1\mathbf{w}\,|\dot{\varphi}_d| + \mathbf{C}_4\,|\dot{\mathbf{q}}_m| + \mathbf{C}_5\,|\ddot{\mathbf{q}}_m(\mathbf{B}_{p,max})|\ \big] \le \mathbf{K}.$$

It is clear that the motor velocity and current are the main factors in finding the maximum values for the left-hand side of inequality (33). Since we already know the current $\mathbf{I}_m$ and motor velocity $\mathbf{q}_m$ is bounded, the variables i.e., $\mathbf{K}$, $\mathbf{C}_4$ and $\mathbf{C}_5$, should be chosen properly to keep always the sliding controller in stable convergence while the energy-based controller varies $\left(\mathbf{q}_{s,d}, \mathbf{B}_p\right)$ parameters internally.

One of the key tasks of the proposed sliding controller is to adjust the desired deflection angle $\mathbf{q}_{s,d}$ to align/contact the inflatable pipe d_p diameter with the spiral spring line d_s, which needs to be tuned based on the change in $\mathbf{q}_s(t)$. When there is a gap between d_p and d_s in the radial axis (i.e., $d_s > d_p$), the energy-based controller for inflatable pipes can become ineffective (see Fig. 5 for details), as the inflated damping pipes with existing gaps may not generate enough friction or impact force to deflect the spring. To address this issue, we have designed the sliding-mode controller in such a way that the springs are deflected relative to each other based on the computed distance gap and given disturbance, in order to compensate for this gap. Since there is no direct sensory input available to measure the distance between the two lines of the spiral spring, we approximate it from a discretized model of (9) for the i-th spring, as follows

$$m_{\rho,i}\frac{\Delta\dot{r}_{s,i}(k)}{T} - m_{\rho,i}r_{s,i}\left(\frac{\Delta\theta_i(k)}{T} - \frac{\Delta\varphi(k)}{T}\right)^2 + B_{r,i}\frac{\Delta r_{s,i}(k)}{T} + K_{r,i}r_{s,i}(k) = 0, \tag{33}$$

where $\Delta\dot{r}_{s,i}(k) = \dot{r}_{s,i}(k) - \dot{r}_{s,i}(k-1)$, $\Delta r_{s,i}(k) = r_{s,i}(k) - r_{s,i}(k-1)$, $\Delta\theta_i(k) = \theta_i(k) - \theta_i(k-1)$ and $\varphi_i(k) = \varphi_i(k) - \varphi_i(k-1)$. One by knowing that $q_{s,i}(k) = \theta_i - \varphi$ the model can be re-ordered for $\Delta q_{s,i}(k)$ as

$$\Delta q_{s,i}^2(k) = \frac{T}{m_{\rho,i}r_{s,i}(k)}\big[m_{\rho,i}\Delta\dot{r}_{s,i}(k) + B_{r,i}\Delta r_{s,i}(k) + T\cdot\ K_{r,i}r_{s,i}(k)\big]. \tag{34}$$

Since we have two models (34) for each motor and we need to determine the relevant difference between the two motors in order to obtain the desired deflection, we subtract the models

$$q_{s,d}(k) = q_{s,1}(k-1) - q_{s,2}(k-1) + \left[\left(\frac{T}{m_{\rho,1}r_{s,1}(k)}\right)\big[m_{\rho,1}\Delta\dot{r}_{s,1}(k)B_{r,1}\Delta r_{s,1}(k) + T\ k_{r,1}r_{s,1}(k)\big]\right]^{\frac{1}{2}} - \left[\left(\frac{T}{m_{\rho,2}r_{s,2}(k)}\right)\big[m_{\rho,2}\Delta\dot{r}_{s,2}(k) + B_{r,2}\Delta r_{s,2} + T\ k_{r,2}r_{s,2}(k)\big]\right]^{\frac{1}{2}}$$

Finally, we can divide the desired deflection (35) equally, with assumption of equal amount of angular deviation for each motor, between the motors:

$$\mathbf{q}_{s,d}(k+1) = \begin{cases} \begin{bmatrix} +q_{s,d}/2 & 0 \\ 0 & -q_{s,d}/2 \end{bmatrix}, & q_{s,d} > 0 \\ \begin{bmatrix} -q_{s,d}/2 & 0 \\ 0 & +q_{s,d}/2 \end{bmatrix}, & q_{s,d} \le 0 \end{cases} \tag{35}$$

Note that when $q_{s,d} > 0$ mean expansion of spiral springs and $q_{s,d} \le 0$ compression of the spiral springs.

IV. Experiment Results

In this section, we evaluate the behavior of the SPIRO mechanism in various cases to determine its performance and evaluate the abilities of the system. Different motion scenarios are chosen to assess the performance of the introduced adaptive impedance controller. Table I presents the parameters for the SPIRO mechanism and the proposed energy-based-sliding-mode controller. The double-sided spiral spring stiffness constant $\mathbf{K}_c$ is determined with tests as shown in Fig.

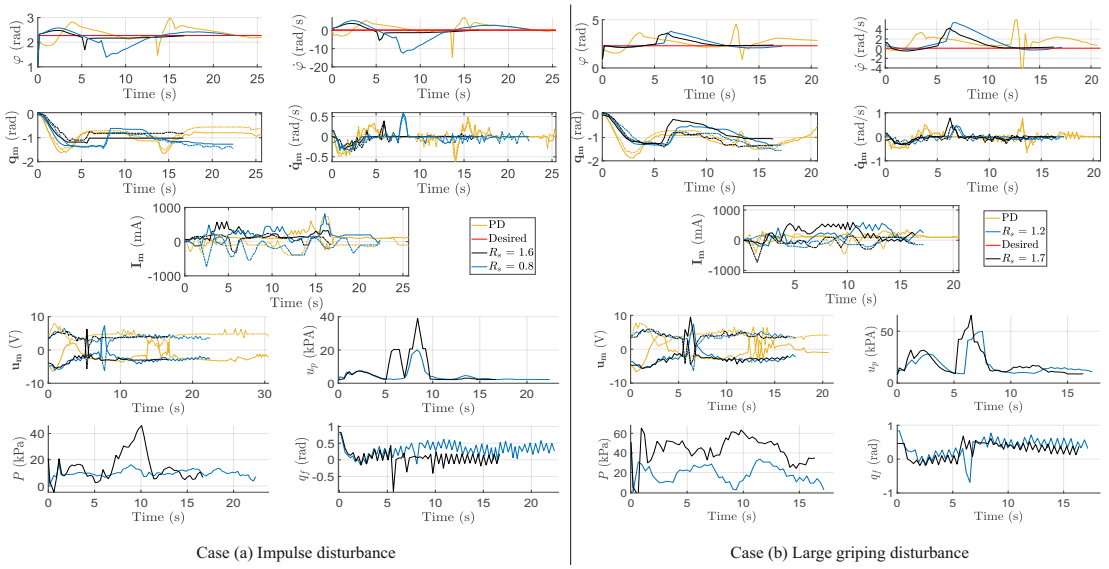

Fig. 8. (a) Results for impulse disturbances, (b) Results for large gripping disturbances. The same results captured from experiment video.

4 [36]. Damping constant $\mathbf{B}_c$ is approximated with value that exists when there is not pressure in inflatable pipes. $\{\mathbf{K}_r, \mathbf{B}_r\}$ are the mass-point impedance profile approximation values from experimental tests in axial direction as shown in Fig. 5. The DC motor characteristics are elaborated for the rest of parameters. The controller operates according to the block diagram shown in Fig. 7, utilizing Eqs. (25), (30), and (35).

A. The Point-to-point Performance

At first, we check the point-to-point convergence. In this study, we have chosen the initial states as $\boldsymbol{x}_0 = \big[-\pi/4,\ 0,\ 0,\ r_a,\ r_a\ \big]$, $\boldsymbol{x}_{m,0} = \big[0,\ 0,\ 0,\ 0\big]$, and the desired states for the SPIRO mechanism are given as follows $\{\varphi_d,\ \dot{\varphi}_d,\ \mathbf{I}_{m,d}\} = \{2.3,\ 0,\ 0, 0\}$. In this part, we look for two different cases: 1. fast and sharp impulse disturbances, 2. large deviations through gripping. The evaluation happens by comparing the conventional tuned PD controller and our proposed strategy in different softness ratio R_s of the adaptive damper by energy-based controller $\mathbf{u}_p$. To clarify, the PD controller is tuned to converge the link of the SPIRO mechanism using the motor rotations $\mathbf{u}_m$ only that connects through the double-sided spring and damping inflatable pipes has constant inflation $P \in$[5-10] kPA.

TABLE I
SPIRO MECHANISM AND CONTROLLER PARAMETERS .

Variable	Value	Variable	Value
$\mathbf{R}_m$	1.02 $\mathbf{I}_{2\times2}$ Ω	$\mathbf{K}_r$	0.6 $\times10^{-3}$ $\mathbf{I}_{2\times2}$ N/rad
$\mathbf{L}_m$	0.0576 $\mathbf{I}_{2\times2}$ mH	$\mathbf{B}_r$	0.1 $\times10^{-3}$ $\mathbf{I}_{2\times2}$ Ns/rad
$\mathbf{n}$	111 $\mathbf{I}_{2\times2}$	$\mathbf{m}_g$	0.001 $\mathbf{I}_{2\times2}$ kg
$\mathbf{J}'_m$	5.05×10^{-6} $\mathbf{I}_{2\times2}$ kg·m^2	$\mathbf{C}_1$	2.2 $\mathbf{I}_{2\times2}$
$\mathbf{J}_g$	1.282×10^{-6} $\mathbf{I}_{2\times2}$ kg·m^2	$\mathbf{C}_2$	0.02 $\mathbf{I}_{2\times2}$
$\mathbf{K}_c$	0.095 $\mathbf{I}_{2\times2}$ N/rad	$\mathbf{C}_3$	0.005 $\mathbf{I}_{2\times2}$
$\mathbf{B}_c$	0.12 $\mathbf{I}_{2\times2}$ Ns/rad	$\mathbf{C}_4$	0.4 $\mathbf{I}_{2\times2}$
$\mathbf{B}_m$	8.05×10^{-4} $\mathbf{I}_{2\times2}$ Ns/rad	$\mathbf{C}_5$	1.1 $\mathbf{I}_{2\times2}$
$\mathbf{B}_g$	1.282×10^{-5} $\mathbf{I}_{2\times2}$ Ns/rad	$\mathbf{K}$	297 $\mathbf{I}_{2\times2}$
$\mathbf{K}_b$	240×10^{-4} $\mathbf{I}_{2\times2}$ Nm/A	$\mathbf{k}_e$	3 $\mathbf{I}_{2\times2}$
$\mathbf{A}_p$	0.0103 $\mathbf{I}_{2\times2}$ m^2	$\mathbf{k}_d$	5 $\mathbf{I}_{2\times2}$
$\mathbf{r}_a$	0.044 $\mathbf{I}_{2\times2}$ m	$\mathbf{k}_p$	4 $\mathbf{I}_{2\times2}$
$L_{s,i}$	0.12 m	l_l	0.11 m
$n_{s,i}$	7.04	l_e	0.03 m
d_t	0.0015 m	d_{safe}	0.0014 m
r_m	0.0041 m	m_l	0.5 kg
b_s	0.0117 m	m_e	0.25 kg

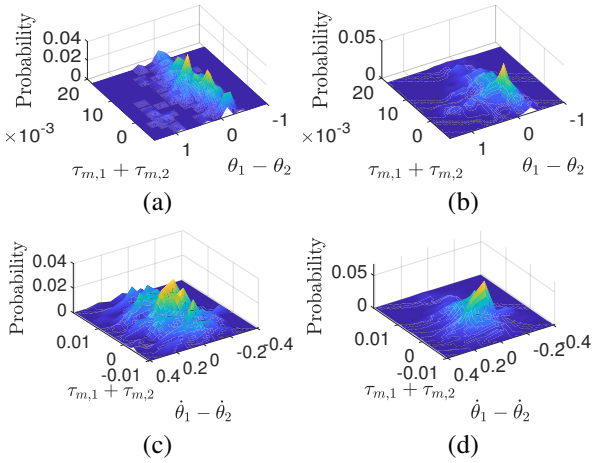

Fig. 9. Stiffness and damping profiles for stiff and soft modes with various disturbance ranges: a) The exerted torque versus the relative angular deflection in soft mode b) The exerted torque versus the relative angular deflection in stiff mode c) The exerted torque versus the relative angular velocity in soft mode d) The exerted torque versus the relative angular velocity in stiff mode

In the first case, the example results are depicted in Fig. 8-a [2]. After the link of the SPIRO mechanism reaches a steady-state, an impulse is applied to the link. With the PD controller, significant fluctuations and overshoot are observed before eventually converging to the desired values. This behaviour indicates that managing the spring stiffness is challenging when ignoring the dynamic properties of the SPIRO mechanism, particularly the deflection angle. Next, the proposed controller is evaluated with different softness ratios. The results demonstrate that SPIRO exhibits improved disturbance rejection for both R_s values. However, when the softness ratio is higher, i.e., $R_s = 1.6$, the disturbance in the link's states $[\varphi, \dot{\varphi}]$ is mitigated more effectively with minimal overshoot, attributed to the higher effect of the damping profile. It is worth noting that a higher value of R_s does not necessarily imply

[2]The video demonstration shows the experiment.

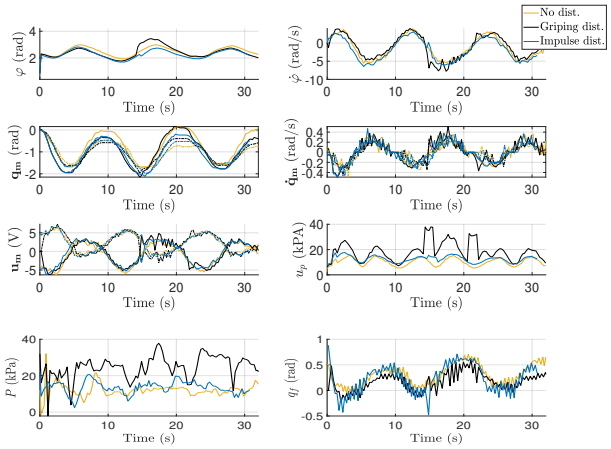

Fig. 10. The swing motion results.

a stiffer or more rigid motion, which confirms the adaptive impedance profile.

In addition, the proposed controller operates as expected by monitoring the relative angular deflection $(\theta_1 - \theta_2)$ between the motors' orientations $\mathbf{q}_m$. When a disturbance is applied, the angular orientation of the motors generates a relative deflection to conserve the introduced energy of the disturbance. Furthermore, as the softness ratio R_s increases, the damping ratio limits the magnitude of larger relative deflections, as evidenced in the case of $R_s = 1.6$. In contrast, with the PD controller, this property is not prominent, and motors at both ends tend to work similarly, resulting in internal velocity fluctuations. As the softness ratio R_s decreases, the convergence time becomes longer since the controller aims to minimize fluctuations for safety reasons during human interaction and utilises the deflected springs energy more. On the other hand, larger values of R_s result in quicker and more accurate convergence. Additionally, the results show the control inputs $\mathbf{u}_m, u_p$, indicating that the motor burden is reduced when the variable damping via u_p is more active. In addition, the energy-based-sliding-mode controller effectively modulates the pressure in the inflatable pipes P to adapt the damping profiles and relative desired deflection angle q_f. It is important to note that in this setup, both spring's inflatable pipes are connected together, resulting in a single pressure.

The next case involves a more challenging scenario where a human grips the link and applies a long-lasting force to deviate the link states deliberately. The results are presented in Fig. 8-b. It is evident from the angular orientation and velocity of the link that the PD controller generates a significant reaction torque, causing the link to rapidly and uncontrollably come down (as shown in the video), posing serious risks. Moreover, the deformation of the spring also leads to a drift in the proper steady-state convergence of the PD controller. In contrast, our proposed controller dissipates the energy transferred due to the disturbance smoothly and flawlessly by effectively managing the spring energy. Notably, in cases of lower softness ratios (R_s) (i.e., higher stiffness), the desired deflection value can reach as high as 1 rad due to the effect of the disturbance. However, the adaptive damping profile of our controller with higher R_s values can significantly reduce this deflection angle to less than 0.3 rad with minor fluctuations. The sensitivity of the PD controller to large disturbances is also evident from the motor control inputs $\mathbf{u}_m$ that occur in the time interval $t \in [12\text{-}15]$ s.

To clearly demonstrate the capability of the SPIRO mechanism with the energy-based sliding-mode controller, we conducted an extensive experiment with varying disturbance levels for both soft and stiff modes. We considered R_s values in the range of $[0.6 - 1.1]$ for the soft mode and $[1.2 - 2.2]$ for the stiff mode. Please note that the experiment was conducted with angular disturbances ranging from $[0, \pi/4]$ rad for impulse and $[0, \pi/2]$ rad for gripping forms, involving a maximum direct force of 15 N. We performed over ten experiments for each mode with different disturbance levels, assuming a standard Gaussian distribution for the applied forces. The results of these experiments are summarized in Fig. 9. The plot depicts the stiffness and damping profiles expressed in the 3-D manifold as a function of the probability. The probability distribution pattern clearly indicates that the relative stiffness behaviour changes significantly based on the choice of the adaptive damper profile (R_s). This validates that our proposed strategy can dynamically adjust the stiffness profile based on the task requirements. For instance, in the stiff mode, when a more significant torque $\tau_{m,1} + \tau_{m,2}$ is exerted on the double-sided spiral spring, the relative angular deflection $\theta_1 - \theta_2$ is smaller. On the other hand, the soft mode allows for more flexibility in deflection angles. A similar pattern is observed for the relative damping profile, which depicts the relationship between the relative angular velocity $\dot{\theta}_1 - \dot{\theta}_2$ and the exerted torque $\tau_{m,1} + \tau_{m,2}$. The probability distribution for damping also changes significantly between the soft and stiff modes. This provides evidence that our proposed controller with adaptive impedance can exhibit a wide range of stiffness and damping variations based on the specific scenario, problem, or task requirements.

B. The Swing Motion

In the last case, we check the performance of the SPIRO mechanism in the swing motion. The initial states are considered as same as in the previous case. However, we assign a sine trajectory and its derivative for the link to follow as $[\varphi_d(t), \dot{\varphi}_d(t)]$ where $\varphi_d(t) = \varphi_{d,0} + \lambda_\varphi \sin(\omega_\varphi\, t)$ where $\varphi_{d,0}$, λ_φ and ω_φ are the initial angle, the gain/rate of change and angular frequency, respectively.

Fig. 10 presents the performance of the SPIRO mechanism with three different strategies. In the first strategy, the controller is operated in the soft mode without any disturbance. The results demonstrate that the swing motion is executed successfully. The impulse and gripping disturbance responses for the rest of the experiments demonstrated satisfactory convergence (please refer to the video presentation). An interesting observation is the energy-based controller that dynamically adjusts the pressure (adaptive damping and robust stiffness) based on the angular orientation of the link. Specifically, as the angle with respect to gravity increases to minimize fluctuations due to stiffness, the pressure also increases. And, when the link comes down, the double-sided spring is deflected to increase the potential energy for an easier transition when links expect to rise.

V. Conclusion

In this paper, we introduced "SPIRO", a novel compliant actuator with a compact mechanism design that includes a variable stiffness profile using a spiral spring design and a variable damping profile with inflatable soft pipes. The unique feature of SPIRO is its ability to interchangeably change the stiffness and damping profiles with independent control inputs, making it highly versatile. Also, SPIRO has a compact design that can be easily implemented in conventional electric motors. To fully utilize the capabilities of SPIRO as a variable impedance actuator (VIA), we also proposed

a new energy-based-sliding-mode controller with an adaptive variable impedance, based on the disturbance energy. The proposed controller opens up possibilities for versatile and adaptable actuator performance, offering the potential for various applications in robotics, exoskeletons, and other fields.

REFERENCES

[1] M. Hutter, "Starleth & co.: Design and control of legged robots with compliant actuation," Ph.D. dissertation, ETH Zurich, 2013.

[2] S. Monteleone, F. Negrello, M. G. Catalano, M. Garabini, and G. Grioli, "Damping in compliant actuation: A review," *IEEE Robotics & Automation Magazine*, 2022.

[3] M. Howard, D. J. Braun, and S. Vijayakumar, "Transferring human impedance behavior to heterogeneous variable impedance actuators," *IEEE Trans. Robot.*, vol. 29, no. 4, pp. 847–862, 2013.

[4] Y. Ning, H. Huang, W. Xu, W. Zhang, and B. Li, "Design and implementation of a novel variable stiffness actuator with cam-based relocation mechanism," *Journal of Mechanisms and Robotics*, vol. 13, no. 2, 2021.

[5] Z. Niu, M. I. Awad, U. H. Shah, M. N. Boushaki, Y. Zweiri, L. Seneviratne, and I. Hussain, "Towards safe physical human-robot interaction by exploring the rapid stiffness switching feature of discrete variable stiffness actuation," *IEEE*, vol. 7, no. 3, pp. 8084–8091, 2022.

[6] M. Cestari, D. Sanz-Merodio, J. C. Arevalo, and E. Garcia, "An adjustable compliant joint for lower-limb exoskeletons," *IEEE/ASME Transactions On Mechatronics*, vol. 20, no. 2, pp. 889–898, 2014.

[7] D. Wang, K.-M. Lee, and J. Ji, "A passive gait-based weight-support lower extremity exoskeleton with compliant joints," *IEEE Trans. Robot.*, vol. 32, no. 4, pp. 933–942, 2016.

[8] L. Liu, B. J. Misgeld, A. Pomprapa, and S. Leonhardt, "A testable robust stability framework for the variable impedance control of 1-dof exoskeleton with variable stiffness actuator," *IEEE Trans. Control Syst. Technol.*, vol. 29, no. 6, pp. 2728–2737, 2021.

[9] Z. Dong, J. V. S. Luces, A. A. Ravankar, S. A. Tafrishi, and Y. Hirata, "A performance evaluation of overground gait training with a mobile body weight support system using wearable sensors," *IEEE Sens. J.*, vol. 23, no. 11, pp. 12 209–12 223, 2023.

[10] S. Wolf, G. Grioli, O. Eiberger, W. Friedl, M. Grebenstein, H. Höppner, E. Burdet, D. G. Caldwell, R. Carloni, M. G. Catalano *et al.*, "Variable stiffness actuators: Review on design and components," *IEEE/ASME transactions on mechatronics*, vol. 21, no. 5, pp. 2418–2430, 2015.

[11] A. Bicchi and G. Tonietti, "Fast and" soft-arm" tactics [robot arm design]," *IEEE Robotics & Automation Magazine*, vol. 11, no. 2, pp. 22–33, 2004.

[12] D. J. Braun, F. Petit, F. Huber, S. Haddadin, P. Van Der Smagt, A. Albu-Schäffer, and S. Vijayakumar, "Robots driven by compliant actuators: Optimal control under actuation constraints," *IEEE Trans. Robot.*, vol. 29, no. 5, pp. 1085–1101, 2013.

[13] M. Hutter, C. Gehring, A. Lauber, F. Gunther, C. D. Bellicoso, V. Tsounis, P. Fankhauser, R. Diethelm, S. Bachmann, M. Blösch *et al.*, "Anymal-toward legged robots for harsh environments," *Advanced Robotics*, vol. 31, no. 17, pp. 918–931, 2017.

[14] H. Zhong, X. Li, L. Gao, and C. Li, "Toward safe human–robot interaction: A fast-response admittance control method for series elastic actuator," *IEEE Trans. Autom. Sci. Eng.*, vol. 19, no. 2, pp. 919–932, 2021.

[15] J. Song, A. Zhu, Y. Tu, X. Zhang, and G. Cao, "Novel design and control of a crank-slider series elastic actuated knee exoskeleton for compliant human–robot interaction," *IEEE/ASME Transactions on Mechatronics*, 2022.

[16] X. Zhou and S. Bi, "A survey of bio-inspired compliant legged robot designs," *Bioinspiration & biomimetics*, vol. 7, no. 4, p. 041001, 2012.

[17] M. Laffranchi, L. Chen, N. Kashiri, J. Lee, N. G. Tsagarakis, and D. G. Caldwell, "Development and control of a series elastic actuator equipped with a semi active friction damper for human friendly robots," *Robotics and Autonomous Systems*, vol. 62, no. 12, pp. 1827–1836, 2014.

[18] S. Haddadin, A. Albu-Schäffer, O. Eiberger, and G. Hirzinger, "New insights concerning intrinsic joint elasticity for safety," in *2010 IEEE/RSJ International Conference on Intelligent Robots and Systems*. IEEE, 2010, pp. 2181–2187.

[19] D. J. Braun, V. Chalvet, and A. Dahiya, "Positive–negative stiffness actuators," *IEEE Trans. Robot.*, vol. 35, no. 1, pp. 162–173, 2018.

[20] C. W. Mathews and D. J. Braun, "Design of parallel variable stiffness actuators," *IEEE Trans. Robot.*, 2022.

[21] U. K. Mavinkurve, S. A. Tafrishi, A. Kanada, K. Honda, Y. Nakashima, and M. Yamamoto, "An experimental study on energy-based control of rigid parallel series elastic actuator," in *2021 World Automation Congress (WAC)*. IEEE, 2021, pp. 26–31.

[22] B. Vanderborght, A. Albu-Schäffer, A. Bicchi, E. Burdet, D. G. Caldwell, R. Carloni, M. Catalano, O. Eiberger, W. Friedl, G. Ganesh *et al.*, "Variable impedance actuators: A review," *Robotics and autonomous systems*, vol. 61, no. 12, pp. 1601–1614, 2013.

[23] M. Laffranchi, N. G. Tsagarakis, and D. G. Caldwell, "A variable physical damping actuator (vpda) for compliant robotic joints," in *2010 IEEE Int. Conf. Robot. Autom.* IEEE, 2010, pp. 1668–1674.

[24] R. J. Farris and M. Goldfarb, "Design of a multidisc electromechanical brake," *IEEE/ASME Transactions on Mechatronics*, vol. 16, no. 6, pp. 985–993, 2011.

[25] K. Gunura, J. Bocanegra, and F. Iida, "Design and control of a novel visco-elastic braking mechanism using hma," in *International Conference on Intelligent Robotics and Applications*. Springer, 2011, pp. 416–425.

[26] B. H. Do, I. Choi, and S. Follmer, "An all-soft variable impedance actuator enabled by embedded layer jamming," *IEEE/ASME Transactions on Mechatronics*, 2022.

[27] L. Chen, M. Garabini, M. Laffranchi, N. Kashiri, N. G. Tsagarakis, A. Bicchi, and D. G. Caldwell, "Optimal control for maximizing velocity of the compact compliant actuator," in *2013 IEEE Int. Conf. Robot. Autom.* IEEE, 2013, pp. 516–522.

[28] Y. Pan, H. Wang, X. Li, and H. Yu, "Adaptive command-filtered backstepping control of robot arms with compliant actuators," *IEEE transactions on control systems technology*, vol. 26, no. 3, pp. 1149–1156, 2017.

[29] H. Wang, Y. Pan, S. Li, and H. Yu, "Robust sliding mode control for robots driven by compliant actuators," *IEEE Transactions on Control Systems Technology*, vol. 27, no. 3, pp. 1259–1266, 2018.

[30] S. A. Tafrishi, X. Dai, Y. Hirata, and A. Burns, "Discretization and stabilization of energy-based controller for period switching control and flexible scheduling," in *2022 American Control Conference (ACC)*. IEEE, 2022, pp. 844–849.

[31] M. Harder, M. Keppler, X. Meng, C. Ott, H. Höppner, and A. Dietrich, "Simultaneous motion tracking and joint stiffness control of bidirectional antagonistic variable-stiffness actuators," *IEEE Robot. Autom. Lett.*, vol. 7, no. 3, pp. 6614–6621, 2022.

[32] E. Spyrakos-Papastavridis, P. R. Childs, and J. S. Dai, "Passivity preservation for variable impedance control of compliant robots," *IEEE/ASME Transactions on Mechatronics*, vol. 25, no. 5, pp. 2342–2353, 2019.

[33] Z. Jin, D. Qin, A. Liu, W.-a. Zhang, and L. Yu, "Model predictive variable impedance control of manipulators for adaptive precision-compliance tradeoff," *IEEE/ASME Transactions on Mechatronics*, vol. 28, no. 2, pp. 1174–1186, 2022.

[34] C.-H. Huang, K.-W. Chiao, C.-P. Yu, Y.-C. Kuo, and C.-C. Lan, "A variable-stiffness robot for force-sensitive applications," *IEEE/ASME Transactions on Mechatronics*, 2023.

[35] D. Bennett, J. Hollerbach, Y. Xu, and I. Hunter, "Time-varying stiffness of human elbow joint during cyclic voluntary movement," *Experimental brain research*, vol. 88, pp. 433–442, 1992.

[36] Y. Kim, J. Lee, and J. Park, "Compliant joint actuator with dual spiral springs," *IEEE/ASME Transactions on Mechatronics*, vol. 18, no. 6, pp. 1839–1844, 2013.

[37] J.-S. Chen and I.-S. Chen, "Deformation and vibration of a spiral spring," *International Journal of Solids and Structures*, vol. 64, pp. 166–175, 2015.

Seyed Amir Tafrishi (M'18) received his M.Sc. degree in control systems engineering from the University of Sheffield in 2014, UK, and Ph.D. degree in mechanical engineering from Kyushu University, Japan in 2021.

He is currently Lecturer at Engineering School, Cardiff University, UK. He was a Specially Appointed Assistant Professor working on Mooonshot R & D project JST at Tohoku University, Japan, between 2021-2022. Since 2014, he has been a visiting researcher at University of Sheffield, the Mechatronics Lab at METU, Turkey, and the Fluid Mechanics Lab at the University of Tabriz, Iran. His research interests include robotics, mechanism design, geometric mechanics and under-actuated systems.

Yasuhisa Hirata (M'98) received the B.E., M.E., and Ph.D. degrees in mechanical engineering from Tohoku University, in 1998, 2000, and 2004, respectively.

He is currently a Professor at the Department of Robotics, Tohoku University, Sendai, Japan. He is currently working as a Project Manager of The Moonshot Research and Development Program, JST, an AdCom Member of the IEEE Robotics and Automation Society (RAS), the Associate Vice-President of the Technical Activity Board of IEEE RAS, and the Co-Chairs of IEEE RAS Technical Committee on Rehabilitation and Assistive Robotics. His research interests are passive robots, assistive robots, cooperative robotics and human-robot interaction.